ORIGINAL RESEARCH

The effect of ply properties in paperboard converting operations: a way to increase formability

**Gustav Lindberg** [ID] · **Artem Kulachenko**

Abstract This study addresses the question of how the difference in mechanical properties of the individual layers in a multi-ply commercial paperboard affects the outcome of the tray-forming operation. Two commercially produced paperboards with nearly identical mechanical properties when conventionally tensile tested were considered. These boards are produced on different machines with the same target grammage and density. Despite the similar mechanical properties, their performance in a given tray-forming operation was drastically different, with one of the boards showing an unacceptable failure rate. To investigate the difference seen during converting operations, a detailed multi-ply finite element model was built to simulate the converting operation. The present model considers a critical area of the paperboard known to exhibit failures. To derive the constitutive relations for each ply in the sub-model, both boards were split to single out individual plies which were then tensile tested. Including the properties of individual plies revealed large differences between the boards when it comes to the distribution of the properties in the thickness direction. In particular, the top plies differed to a large extent. This is attributed to the difference in refining energies for the plies. The results from the three-ply sub-model demonstrated the importance of including the multi-ply structure in the analysis. Weakening of the top ply facing the punch by using lower refining energy considerably increased the risk of failure of the entire board. These results suggest that there is room for optimizing the board performance by adjusting the refining energy at the ply level.

G. Lindberg (✉) · A. Kulachenko
Department of Engineering Mechanics, KTH Royal
Institute of Technology, Stockholm, Sweden
e-mail: gulindbe@kth.se

Graphical abstract
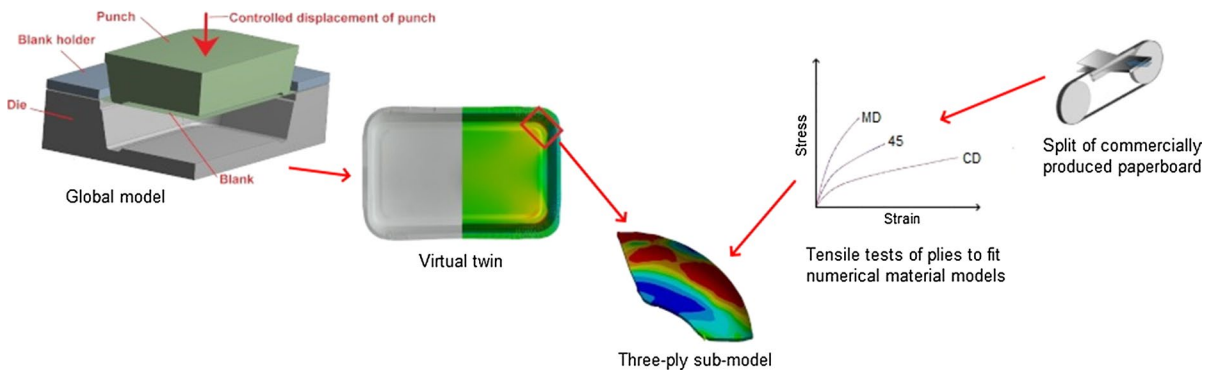
Introduction

The pressure of reducing the use of plastics creates opportunities for the use of paperboard in producing products like plates, food trays, cups, and other containers (Hagman et al. 2017; Rhim 2010; Vishtal and Retulainen 2012). This requires that the board undergoes forming operations. Compared to plastics and sheet metal, paperboard has lower formability, i.e. can undergo less deformation before failure or experience partial damage. Deep drawing of sheet metal is widely used by many industries (Chen and Lin 2007; Reddy et al. 2019; Rojek et al. 2004). Similarly, plastics are used to form a variety of trays and containers (Gill et al. 2020; Siracusa et al. 2008). At the same time, the effort to increase the formability of paperboard and improve the processes enabling the forming operation is ongoing, since paperboard is an important part of shifting towards a circular bioeconomy (Wang et al. 2021).

There are several types of forming operations for paperboard, such as hydroforming, press (tray) forming, deep drawing and molding. The first three of them are all variants of pressing down a sheet of paper or paperboard, called the blank, into a die. Hydroforming presses the blank downwards utilizing air pressure. The press forming uses a punch, also called male die, to press the blank into the bottom of a die, while deep drawing uses the punch to press the blank into a bottomless die (Hagman et al. 2017; Östlund 2017). Complex products such as egg packages are molded (Didone et al. 2017).

Fig. 1 The failed corner during the converting operation using Board A (Lindberg and Kulachenko 2021)

(a)   (b)
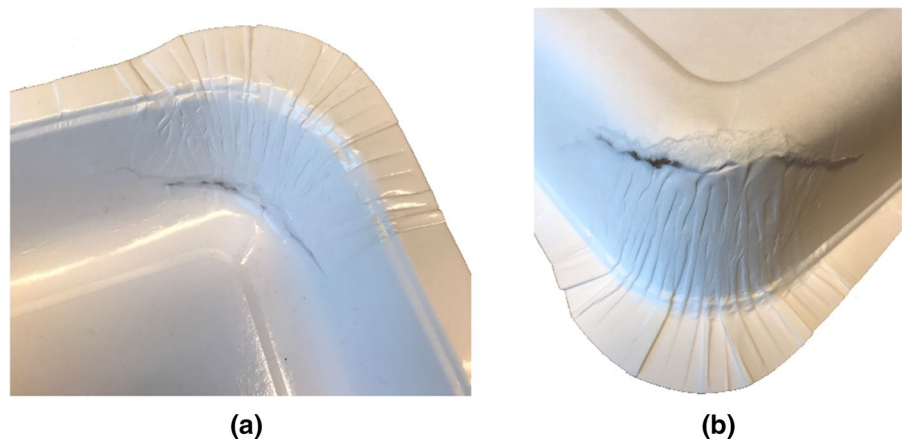
As a part of the product development process using paperboard, simulations of the forming operations can be used. With such simulations, the impact of the paperboard properties on the risk of failure during forming operations can be assessed.

The current study is a continuation of the work performed in Lindberg and Kulachenko (2021), where the tray forming operation was simulated using an implicit non-linear finite element (FE) model using a single-ply approach. In contrast to that previous study, where the difference between the boards can be seen already on the sheet level, the boards considered here have similar properties, but still show of differences in performance. The paperboards are produced on two separate board machines, and are herein called Board A and Board B. It is desirable that both machines can produce identical paperboard, i.e. that Board A and Board B are identical. At the time of the study, however, only Board B had no reported problems at the customer end. In Lindberg and Kulachenko (2021), the tensile tests showed observable differences between the two boards on the sheet level, with Board B having higher stress and strain to failure in the paperboard machine direction (MD) and the cross-machine direction (CD), but somewhat lower stress and strain to failure in the 45-direction. The FE-model in that study predicted that the observed differences on the sheet level can explain the performance degradation in Board A. The model was also capable to predict the position of the failure.

The current study was initiated after the refining energies for Board B were modified in the process development trials which eliminated the differences between the two boards in the tensile tests. I.e., now Board B only had slightly larger strength and strain to failure compared to Board A, such that the difference no longer had a significant role. Board A remained unchanged. Despite the modified refining energies, no problems were reported for this new version of Board B. This raised the question of whether there is any other difference that can explain the degradation in performance of Board A. To advance the investigation, the current study focused on the individual plies of the boards and their effect on the paperboard behavior in the tray forming operation. For this, a three-ply FE sub-model was built where the plies were modeled with their individual material properties and thicknesses. The model is a sub-model of the model in Lindberg and Kulachenko (2021). The sub-model is simulating the area constituting the critical lower corner in the tray forming process, see Fig. 1. As a part of obtaining the numerical material models for the plies, the two boards were split into their plies, and then tensile tested in MD, CD and the 45-direction. Already at that stage, differences were discovered, where foremost the top plies of the two boards had large differences in the tensile test curves. The Board A top ply was considerably weaker than the Board B top ply, and at the same time the Board A bottom ply was very stiff. This difference appeared due to various refining energies used for the pulps. For example, the top ply of Board A had much lower refining energy than its bottom ply, meanwhile, the Board B top and bottom plies had very balanced refining energies, i.e. the outer plies had about the same level of refining energy.

The effect of the refining energy on cellulose material is a very well investigated research field (Jele, Lekha and Sithole 2021). The refining energy affects the number of contacts between the fibers, which affects the tensile properties of paperboard as well as reinforcing the fiber joints in the network due to added fine content (Motamedian, Halilovic and Kulachenko 2019). Most importantly, refining energy is one of the tools which the manufacturer can leverage. Hence, its impact on the forming operation through the changes to the ply properties is of utmost interest. During converting operations, wrinkling of the paperboard in specific locations, such as corners, is a necessary part of the forming process. In experiments, it has been seen that refined fibers make significantly higher wrinkle strength, but at the same time that high refining energy lowers the 3D formability of paperboard (Hauptmann et al. 2015). To increase the formability, it has been suggested that softwood pulp could partially replace the more common birch kraft in paperboards designed for 3D forming applications (Laukala et al. 2019). It has also been suggested that adding gelatin and agar to the pulp could increase the formability of the final paperboard (Vishtal et al. 2015).

Although this work focuses on the impact of the material, it is important to recognize that the forming process has a large impact on the quality of the forming which was shown in a number of publications. For example, the selection of the forming force in the combination of the blank holding force has a great impact on the quality of the formed

products (Leminen, et al. 2018a, b). In addition, the mold temperature and the dwell time were also shown to be important factors affecting the dimensional stability of the tray after forming operations, which is manifested through preservation of the desired geometry after forming (Niini et al. 2021). The plastic-coated substrate can particularly benefit from the temperature optimization, that can help to improve formability and achieve accurate tray dimensions making shorter, less visible wrinkles at the tray corners (Leminen et al. 2020; Ovaska et al. 2018). The rapturing propensity can be reduced through modifying the blank speed and acceleration (Tanninen et al. 2018). Varying the blank holding force during the forming process and, in particular, reducing it toward the end of the forming process

can help preventing the rapture (Tanninen et al. 2020). On the material side, the creasing and perforation (when it is permissible) was shown to have impact on the forming operation and therefore can be used in optimization with the idea to increase the stretchability and minimize the damage in the highly compressed region (Leminen, et al. 2018a, b; Leminen et al. 2019).

Simulations of deep drawing and tray forming of paperboard have been used previously (Awais et al. 2017; Linvill et al. 2017; Wallmeier et al. 2015), with different numerical approaches and objectives. However, the current approach with a multi-ply model for large deformation of paperboard in converting operations has never been done before. With this multi-ply
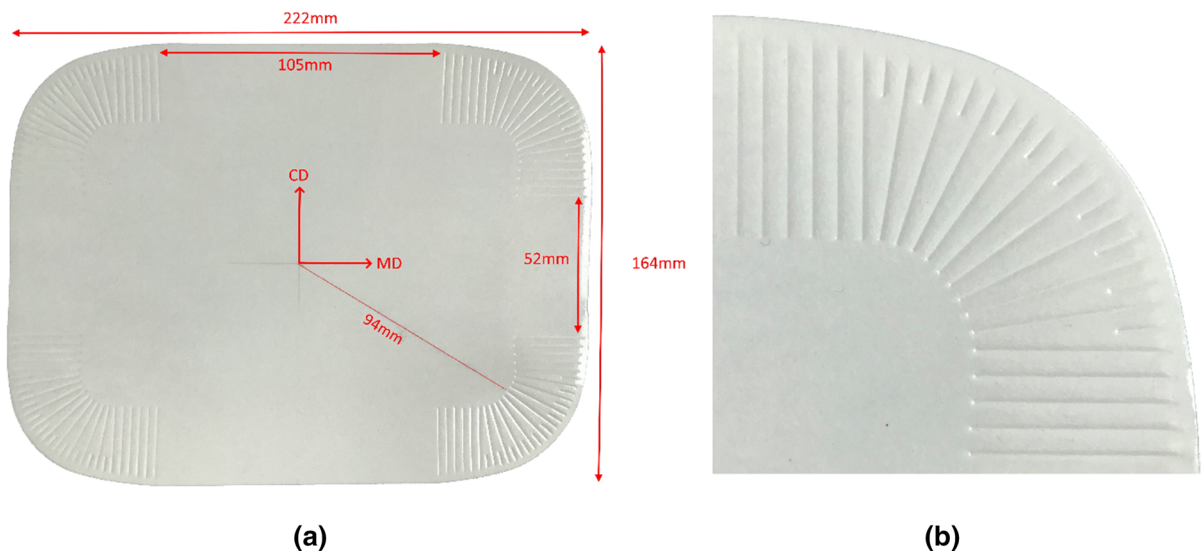
Fig. 2 The paperboard blank before forming operation. **a** The full blank with dimensions and b)\ close-up of the creases (Lindberg and Kulachenko 2021)

Fig. 3 The studied tray after a successful forming operation. In **a** seen slightly from above and in **b** seen from the side (Lindberg and Kulachenko 2021)

Fig. 4 Illustration of the splitting process using a Fortuna Splitting Machine

model, we show how the formability can be improved for a commercially produced paperboard.

The advances with the current study are:

a) The inclusions of the individual ply properties in the modeling of converting operations;

b) Using a sub-modelling approach allowing a more detailed investigation of the critical areas in tray forming;

c) Presenting the evidence of the importance of the multi-ply structure for the formability of the boards.

Materials and methods

The approach in this study was to perform tensile tests of the split and unsplit paperboards, followed by numerical simulations of the critical lower corner of the tray. With the tensile tests of split paperboards, we derived constitutive relations for each ply and assigned them to the numerical model.

The geometry of the tray

In Fig. 2 the paperboard blank is shown as it is prepared by the tray manufacturer for the forming operation. The blank is laminated with a polymer that is extruded over the blank since the tray must withstand moisture during usage. The creasing pattern containing 30 creases in each corner has been impressed on


Fig. 5 Sketch showing the tensile test, with the force F [N] pulling the specimen, and the round markers which are being tracked by the optical tracking system
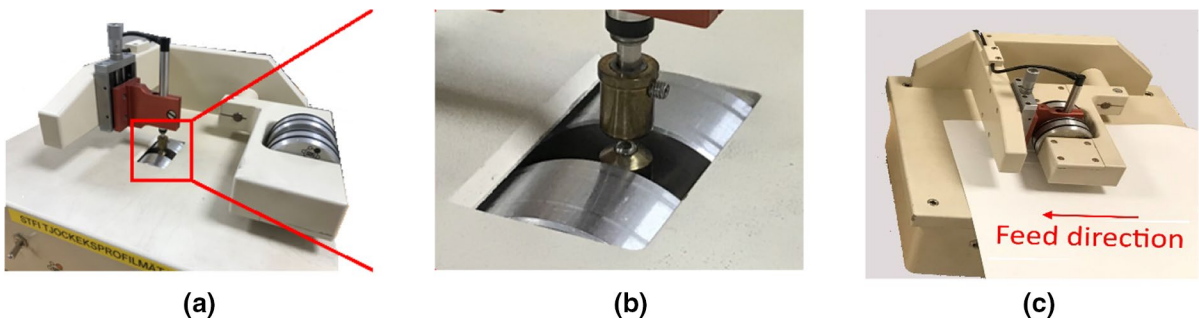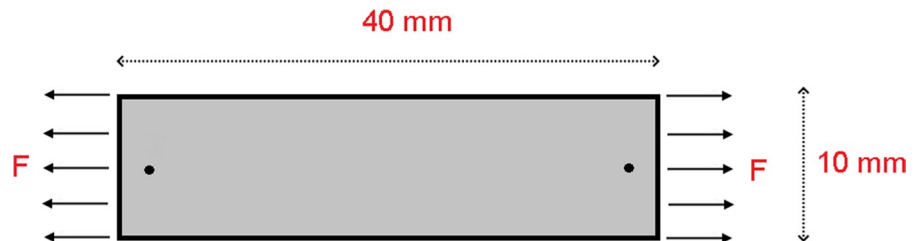
Fig. 6 The STFI Thickness Tester M201 used to measure the thickness of the plies. In **a** and **b** the instrument shown before the paperboard is being fed through it, and in **c** during thickness measurements

Table 1 Results from the thickness measurements of the individual plies

Ply	Mean thickness (µm)	Thickness standard deviation (µm)	Density (kg/m³)
Board A top	89	12	830
Board A middle	238*	15	680
Board A bottom	117	8	830
Board B top	103	10	835
Board B middle	239	12	660
Board B bottom	109	9	835
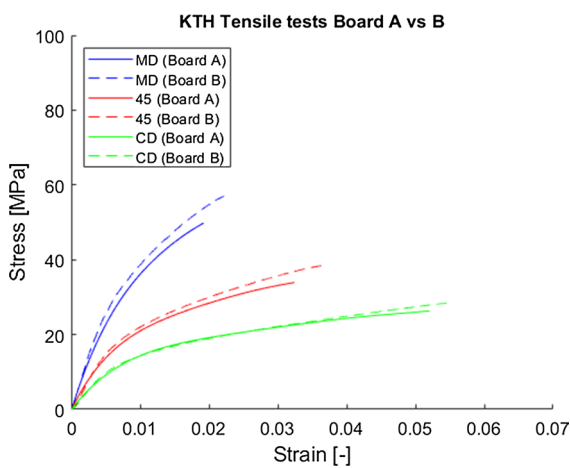
Fig. 7 The tensile tests of the unsplit commercially produced Board A and Board B

the paperboard to facilitate the formation of folds at the corners. The grammage of the paperboards was 330 g/m² and the thickness including the thin (30 µm) and compliant PET (polyethene terephthalate) coating was 0.470 mm. The PET coating is applied on the top ply, i.e. the ply that meets the punch in the tray forming operation. The herein called bottom ply meets the die in the forming operation.
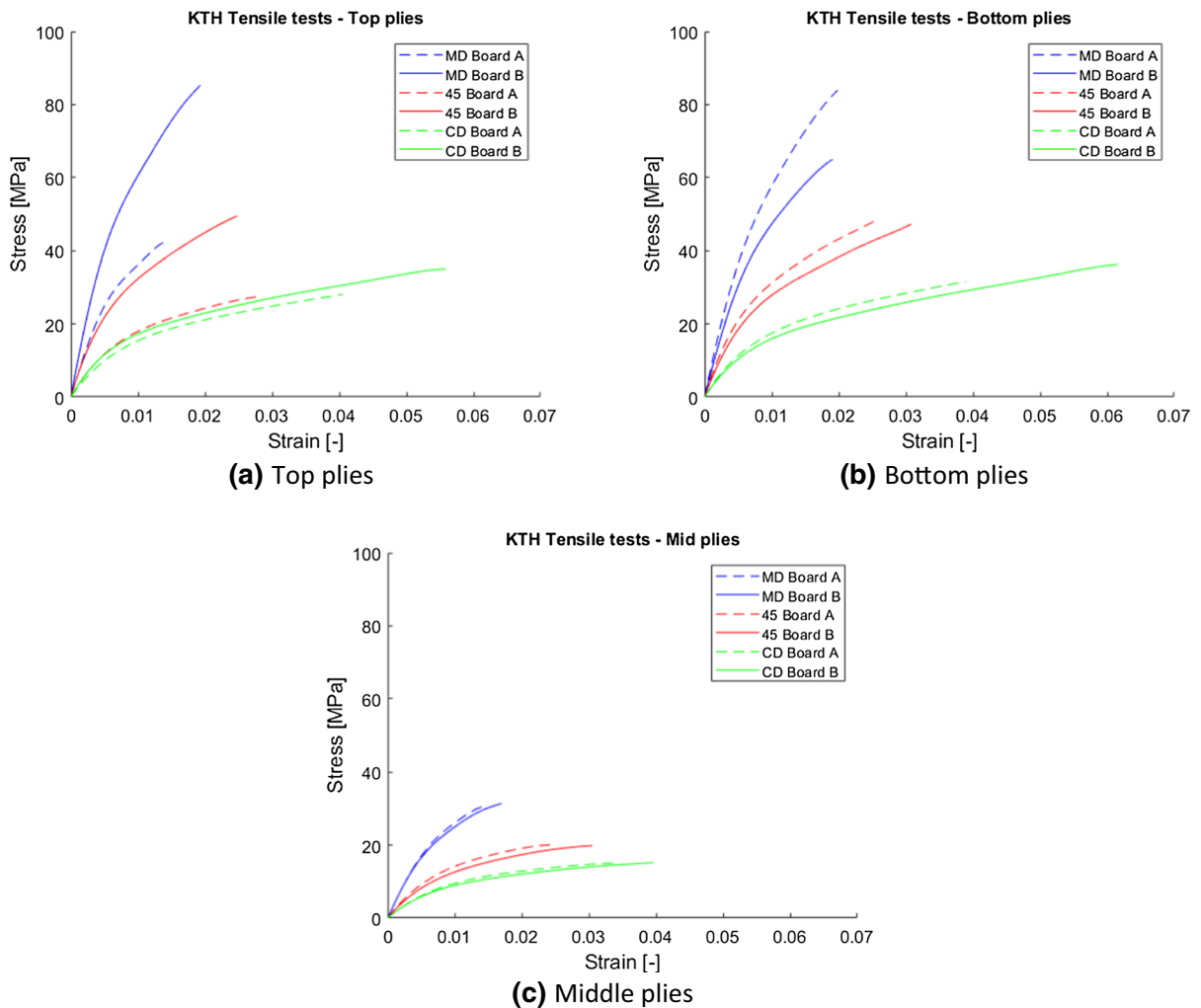
Figure 3 shows the studied tray after a successful forming operation, that is, without detectable failure. The linear dimensions of the formed tray are $185 \times 125 \times 25$ mm.

Board A is a four-ply paperboard, and Board B is a three-ply paperboard. The two middle plies for Board A are identical in their mechanical properties and were treated as one single ply. Hence, both Board A and Board B were simulated as three-ply paperboards.

Tensile tests and thickness measurements

For this study, uniaxial tensile tests of the full boards and the individual plies were conducted at KTH Royal Technical Institute. To avoid laboratory sheets, Board A and Board B were split, i.e. the plies come from commercially produced paperboard (Inverform). The two boards were split using a Fortuna Splitting Machine for paperboard, model AB 320P. The paperboard is fed through two rolls, and a band knife is adjusted to split the board into the desired thickness, as illustrated in Fig. 4.

The tensile tests were prepared by cutting the test specimens into the dimension of 40×10 mm. Specimens were created to be aligned with the paperboard MD, CD, and 45-direction. The specimens were stored for 48 h in a climate-controlled room holding 50% RH and 25 °C (ISO conditions). This procedure was used for both the unsplit boards and the individual plies. The tensile test machine was a Zwick Roell Z1.0, with an optical tracking system of the deformation of the test specimen. The specimen was placed in specially designed grippers which are mounted on the robotic arms pulling the specimen apart. In order to exclude the factor of slippage which may occur between the grippers and the specimen, the optical tracking system was used to register the deformation of the specimen. In Fig. 5 an ongoing tensile test is shown, where the red squares track the spots located on the surface of the test specimen.

Table 2 Mean and standard deviation for the tensile test of the full boards in Fig. 7

Direction	Board A			Board B		
	MD	45	CD	MD	45	CD
Tensile stress Mean value [MPa]	49	34	26	57	38	28
Tensile stress STD [MPa]	1.9	1.7	1.1	2.3	1.1	1.1

Fig. 8 The tensile tests of the individual plies from the two split commercially produced paperboards

The output from the tensile tests is displacement-force curves. To determine the stress curve, the thickness of the plies had to be measured. The measurements were performed using an STFI Thickness Tester M201, which can be seen in Fig. 6. The paperboard is continuously fed through the machine, and a thickness profile is measured. This procedure follows the standard SCAN-P88:01 (Scandinavian Pulp, Paper and Board testing committee. SCAN-P 88:01 2001).

Table 1 shows the results from the thickness measurements of the individual plies. If the mean thickness for the plies is summarized for each board, the

mean thickness for Board A is 444 μm, and for Board B 451 μm. The target thickness for the un-coated paperboards was 440 μm, so the results deviated by 0.9 and 2.5% respectively from the expected.

*Consists of two plies with similar properties.

Figure 7 shows the results of the uniaxial tensile tests performed for the unsplit boards. The tensile tests are performed under ISO standard conditions in three in-plane directions, MD, CD and 45°. Five tests were performed in each direction. The tests in the three in-plane directions enable accurate calibration of the material properties (Alzweighi et al. 2021). As seen in Fig. 7 and Table 2 the two boards have similar

behavior. Board B allows for slightly higher strain and stress to failure. However, when the results from the individual plies are studied, they reveal greater differences between the boards, especially in the top plies. This means that using the unsplit samples does not disclose relevant differences which can explain a drastic change in performance.

Figure 8 shows the uniaxial tensile tests of the individual plies. Here, three tests were performed in each of the three in-plane directions for each ply. As seen, the Board A top ply has a lower strain and stress to failure in all three test directions (MD, 45 and CD) compared to the Board B top ply. The middle plies for both boards have similar behavior and have rather low strain and stress to failure. This is due to the relatively low refining energies for the middle plies. For the bottom ply, Board A has greater stress to failure, but Board B shows a slightly larger strain to failure. Due to a complex load case including both tensile and bending loads, this difference may have significance in the tray forming process despite the fact that the difference is not reflected in the pure tensile tests of the entire boards (Fig. 7).

By comparing Figs. 7 and 8, it is noticeable that the failure strain in, foremost, the 45-direction is higher for the full boards (Fig. 7), than for any individual ply (Fig. 8). This can be explained by two factors. First, certain damage can be introduced as the paperboards are split, which would affect the tensile tests of the individual plies. Another reason could be that a size effect exists through the thickness of paperboard in the same way as it exists for the width (Hagman and Nygårds 2012; Hristopulos and Uesaka 2004; Kulachenko and Uesaka 2012), i.e. that increasing the width of test specimen from small size initially increases the strength and strain to failure before it starts to decrease at larger sizes. This hypothesis is strengthened by studies (I'Anson et al. 2008) showing the same effect by increasing the grammage, where the tensile index increased to then decrease as the grammage was further increased. In Appendix (Fig. 19), the tensile test results for each ply in their respective direction are shown together with the tensile tests of the full board to facilitate the comparison.

Fiber characterization

The pulp going to the two machines have the same retention aids and strengtheners, and very similar mixtures. Hence, to further investigate possible reasons for the difference in performance between the two boards, a quantification of the geometric fiber properties was done during this study. For this, the tool PulpEye was used, which measures the fiber properties in the pulp before going into the paperboard machine. The PulpEye measurements were done on a different occasion than for the production of the paperboards used in the above-described experiments, but, the settings for the refining energies were the same. The results from these measurements show that indeed the fiber composition is very similar between the two boards, and the results are shown in Appendix.

Material description

Paperboard is an anisotropic material, which may be approximated as an orthotropic material. Further, the material also shows different responses in tension and compression. For this stufy, physical tensile tests of the boards were performed, both on the full sheet level and of the individual plies, see Figs. 7 and 8. The results of the tensile tests were used to extrac the input data for the numerical material models.

Paperboard exhibit a reduction in yield limit and strength in compression compared to the corresponding values in tension (Fellers et al. 1980; Xia et al.

Table 3 The elastic material properties for each ply

Ply	Young's modulus E_1 and E_2 (MPa)	Shear modulus G_{12} (MPa)	Poisson's ratio[*] ν_{12} (-)
Board A top	5790, 2599	1130	0.45
Board B top	9590, 3030	3070	0.52
Board A middle	3930, 1540	980	0.47
Board B middle	3940, 1500	860	0.47
Board A bottom	8600, 2863	2970	0.51
Board B Bottom	7030, 2670	2330	0.48

[*]ν_{21} is determined from the above parameters due to the symmetry of the stiffness matrix

2002). This is taken into account by assuming that the yield stress in compression is 70% of that in tension. For the failure evaluation, the compressive strength is reduced by 50% from the tensile value. The chosen values for yield and failure stress levels in compression are based on the reported values in Xia et al. (2002). It is important to note that the failures addressed in this study are exclusively tensile. However, as the failure surface is continuous the compressive part affects it too.

Elastic material properties

In the following theory, the principal material directions MD, CD and ZD are described with indices 1, 2 and 3, respectively. The elastic part of the paperboard is described using Hooke's law $\varepsilon = C\sigma$. For an orthotropic material the full expression reads

$$
\begin{bmatrix} \varepsilon_{11} \\ \varepsilon_{22} \\ \varepsilon_{33} \\ \varepsilon_{23} \\ \varepsilon_{31} \\ \varepsilon_{12} \end{bmatrix} = \begin{bmatrix} \frac{1}{E_1} & \frac{-v_{21}}{E_2} & \frac{-v_{31}}{E_3} & 0 & 0 & 0 \\ \frac{-v_{12}}{E_1} & \frac{1}{E_2} & \frac{-v_{32}}{E_3} & 0 & 0 & 0 \\ \frac{-v_{13}}{E_1} & \frac{-v_{23}}{E_2} & \frac{1}{E_3} & 0 & 0 & 0 \\ 0 & 0 & 0 & \frac{1}{2G_{23}} & 0 & 0 \\ 0 & 0 & 0 & 0 & \frac{1}{2G_{31}} & 0 \\ 0 & 0 & 0 & 0 & 0 & \frac{1}{2G_{12}} \end{bmatrix} \begin{bmatrix} \sigma_{11} \\ \sigma_{22} \\ \sigma_{33} \\ \sigma_{23} \\ \sigma_{31} \\ \sigma_{12} \end{bmatrix}. \quad (1)
$$

The paperboards are modeled with 3D shells with plane stress assumption. In the case of plane stress, the expression in Eq. (1) reduces to

$$
\begin{bmatrix} \varepsilon_{11} \\ \varepsilon_{22} \\ \varepsilon_{12} \end{bmatrix} = \begin{bmatrix} \frac{1}{E_x} & \frac{-v_{21}}{E_y} & 0 \\ \frac{-v_{12}}{E_x} & \frac{1}{E_y} & 0 \\ 0 & 0 & \frac{1}{2G_{12}} \end{bmatrix} \begin{bmatrix} \sigma_{11} \\ \sigma_{22} \\ \sigma_{12} \end{bmatrix}. \quad (2)
$$

The two in-plane values for Young's modulus E_i in Eq. (2) are determined by the fitting procedure, and the in-plane shear modulus G_{12} and Poisson's ratio v_{12} are then calculated using the two separate relations for commercially produced papers (Baum, Habeger and Fleischman 1982)

$$
G_{12} = \frac{\sqrt{E_1 E_2}}{2(1 + \sqrt{v_{12} v_{21}})} \quad \text{and} \quad \sqrt{v_{12} v_{21}} = 0.293. \quad (3)
$$

Equation (3) along with the symmetry condition of the compliance matrix, giving $v_{21}/E_2 = v_{12}/E_1$, give the in-plane elastic material parameters which are listed in Table 3.

The out-of-plane strain ε_{33} can be derived as $\varepsilon_{33} = \frac{-v_{13}}{E_1}\sigma_{11} - \frac{v_{23}}{E_2}\sigma_{22}$ as given by Eq. (1) with $\sigma_{zz} = 0$, but requires estimations of the Poisson's ratios v_{31} and v_{23}.

Hardening model

Plasticity in paperboard has been modeled in many different studies (Alajami et al. 2018; Bedzra et al. 2019; Harrysson and Ristinmaa 2008; Li et al. 2016; Robertsson et al. 2018; Tjahjanto et al. 2015; Xia et al. 2002). The evolution of the plastic strains in the current study is described using Hill's plasticity (Hill 1948), which is suitable for composites and a common way to model plasticity for orthotropic composite such as paperboard. Hill's plasticity is defined as

$$
f(\sigma, \sigma_f) = F(\sigma_{22} - \sigma_{33})^2 + G(\sigma_{33} - \sigma_{11})^2 + H(\sigma_{11} - \sigma_{22})^2 \\ + 2L\sigma_{23}^2 + 2M\sigma_{31}^2 + 2N\sigma_{12}^2 - \sigma_y^2 = 0 \quad (4)
$$

where F, G, H, L, M and N are defined as

Table 4 The Hill parameters for each ply

Ply	R_{11}(-)	R_{22}(-)	R_{33}(-)	R_{12}(-)	R_{23}(-)	R_{13}(-)
Board A top	1.913	1.0	1.051	1.104	1.0	1.0
Board B top	2.809	1.0	1.394	1.723	1.0	1.0
Board A middle	2.216	1.0	1.222	1.375	1.0	1.0
Board B middle	2.244	1.0	1.222	1.348	1.0	1.0
Board A bottom	2.665	1.0	1.299	1.597	1.0	1.0
Board B bottom	2.409	1.0	1.271	1.611	1.0	1.0

$$F = \frac{1}{2}\left(\frac{1}{R_{12}^2} + \frac{1}{R_{33}^2} - \frac{1}{R_{22}^2}\right); \quad G = \frac{1}{2}\left(\frac{1}{R_{33}^2} + \frac{1}{R_{11}^2} - \frac{1}{R_{22}^2}\right); \quad H = \frac{1}{2}\left(\frac{1}{R_{11}^2} + \frac{1}{R_{22}^2} - \frac{1}{R_{33}^2}\right);$$
$$L = \frac{3}{2}\left(\frac{1}{R_{23}^2}\right); \quad M = \frac{3}{2}\left(\frac{1}{R_{13}^2}\right); \quad N = \frac{3}{2}\left(\frac{1}{R_{12}^2}\right). \tag{5}$$

The Hill's parameters R_{ij} in Eq. (5) are defined as

$$R_{11} = \frac{\sigma_{11}^y}{\sigma_y}; \quad R_{22} = \frac{\sigma_{22}^y}{\sigma_y}; \quad R_{33} = \frac{\sigma_{33}^y}{\sigma_y}; \quad R_{12} = \sqrt{3}\frac{\sigma_{12}^y}{\sigma_y}; \quad R_{23} = \sqrt{3}\frac{\sigma_{23}^y}{\sigma_y}; \quad R_{13} = \sqrt{3}\frac{\sigma_{13}^y}{\sigma_y}, \tag{6}$$

and determine the shape of the yield surface, which initial size is determined by the initial yield stresses σ_{ij}^y and the isotropic yield stress σ_y. The material parameters in Eq. (6) are found with the previously mentioned fitting procedure. The stress–strain curve measured in the CD is used as a master curve for the multilinear hardening and the rest of the parameters are fitted in Matlab using the *fmincon*-function to minimize the error between the measured and the calculated tensile test curves. The paperboard is modeled to yield at $R_p = 0.0001$, i.e. the initial yield stress is in this study the stress giving a permanent deformation of 0.01% strain. Such a low value is required to get a good fit between the experimental and the numerical tensile test curves. The quality of the fit is shown in Appendix Fig. 18 for all six plies. The curves on the compressive side are only from the numerical tests since no data is given from experiments. In compression, the two paperboards have a 30% reduction of the yield stress and a 50% reduction of the ultimate stress compared to the tensional side, which renders in the curves on the compressive side in Fig. 18.

The modeled difference in tension and compression for the paperboard plies render in two yield surfaces per ply, one for compression and one for tension. The surface that applies for the current point is determined by the sign of hydrostatic stress. More about the used hardening model is found in Lindberg and Kulachenko (2021). In Table 4, the complete set of parameters for Hill's plasticity used in this study is presented for all plies. Note that the fit of R_{33} is important even though plane stress is approximated, since R_{33} influences the shape of the yield surface in the MD-CD plane.

Failure evaluation

Failure is not included in the numerical model but is evaluated as a part of the post-processing of the final results using the Tsai-Wu stress failure criterion (Tsai and Wu 1971). For plane stress, it reads (Li et al. 2017; Suhling et al. 1985)

$$\sigma_{TW} = F_1\sigma_{11} + F_2\sigma_{22} + F_{11}\sigma_{11}^2 + F_{22}\sigma_{22}^2 + 2F_{12}\sigma_{11}\sigma_{22} + F_{66}\sigma_{12}^2 < 1, \tag{7}$$

where F_i and F_{ij} are defined as

Table 5 The Tsai-Wu parameters for the plies

Ply	F_1 (1/MPa}	F_2 (1/MPa}	F_{11}(1/MPa²)	F_{22}1/MPa²)	F_{66}1/MPa²)	F_{12} (1/MPa)
Board A top	−0.0235	−0.0356	0.0011	0.0025	0.0008	−0.0008
Board B top	0.0352	0.0857	−0.0003	−0.0016	0.0003	−0.0003
Board A middle	−0.0325	−0.0662	0.0021	0.0088	0.0022	−0.0022
Board B middle	−0.0318	−0.0657	0.0020	0.0086	0.0021	−0.0021
Board A bottom	−0.0120	−0.0318	0.0003	0.0020	0.0004	−0.0004
Board B bottom	−0.0154	−0.0276	0.0005	0.0015	0.0004	−0.0004

**(a)** (Lindberg and Kulachenko 2021)   **(b)**
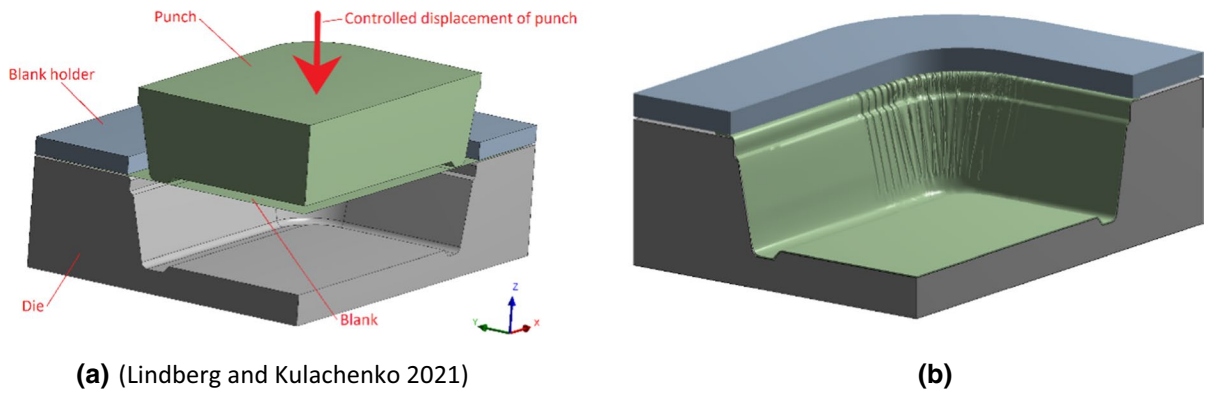
Fig. 9 The quarter model used in the finite element simulation in Lindberg and Kulachenko (2021). In **a** the setup of the model, and in **b** the formed tray at the end of the simulation

(a)   **(b)**
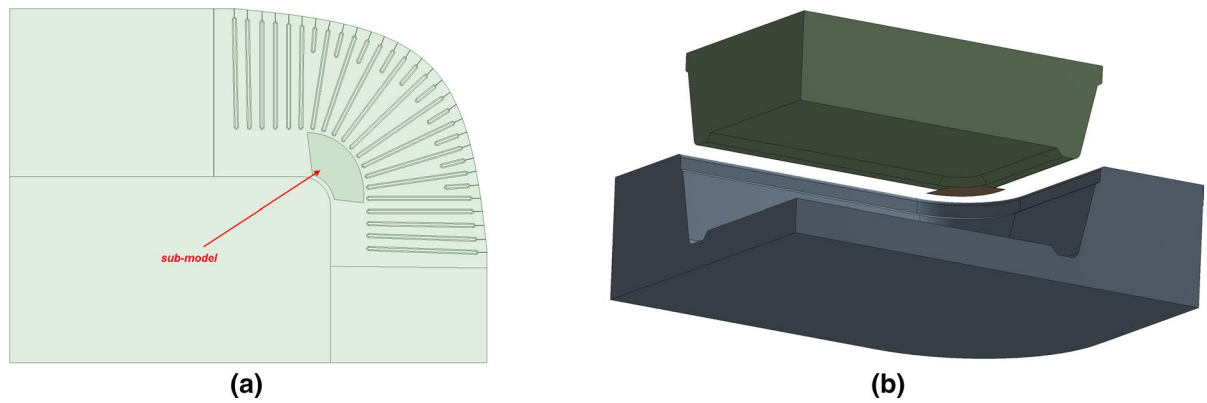
Fig. 10 The sub-model of the critical lower corner, in **a** demonstrated in global model and in **b** the full geometry of the sub-model

Fig. 11 Demonstration of the mapped edge boundary conditions, here showing the mapped displacements
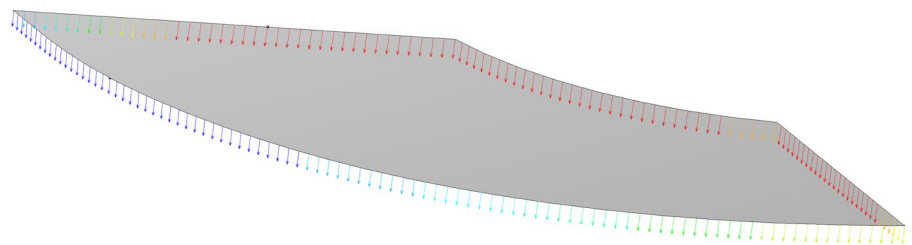
$$F_1 = \frac{1}{\sigma_{11}^t} - \frac{1}{\sigma_{11}^c}; \quad F_2 = \frac{1}{\sigma_{22}^t} - \frac{1}{\sigma_{22}^c}; \quad F_{11} = \frac{1}{\sigma_{11}^t \sigma_{11}^c};$$

$$F_{22} = \frac{1}{\sigma_{22}^t \sigma_{22}^c}; \quad F_{66} = \frac{1}{(\sigma_{12}^t)^2}; \quad F_{12} = k\sqrt{F_{11}F_{22}}, \quad (8)$$

and the indices "t" and "c" are for ultimate tensile stress and ultimate compressive stress respectively. In Eq. (8), F_{12} and the in-plane ultimate shear stress σ_{12}^t require some extra attention. These cannot be directly determined from tensile and compressive tests and require shear testing where the failure envelope is studied. For the current study, no such data is given for the two paperboards. Some estimations from the literature are required. For F_{12} the constant k is chosen as $k = -0.5$, which is suitable

for most composites (Li et al. 2017; Tsai 1984). In Li et al. for the interested reader, F_{12} is analyzed not only for closed failure surfaces but also for open surfaces. The ultimate shear stress σ_{12}^t in Eq. (8) may be estimated by using the geometrical mean of the tensile strength values in MD and CD, as done by Fellers (Fellers, Westerlind and De Ruvo 1983) for evaluation of the compressive modes. This study utilizes the geometrical mean for the tensile modes as

$$\sigma_{12}^t = \sqrt{\sigma_{11}^t \sigma_{22}^t}. \quad (9)$$

In Table 5 sthe material parameters for the failure evaluation are listed, which are given by the
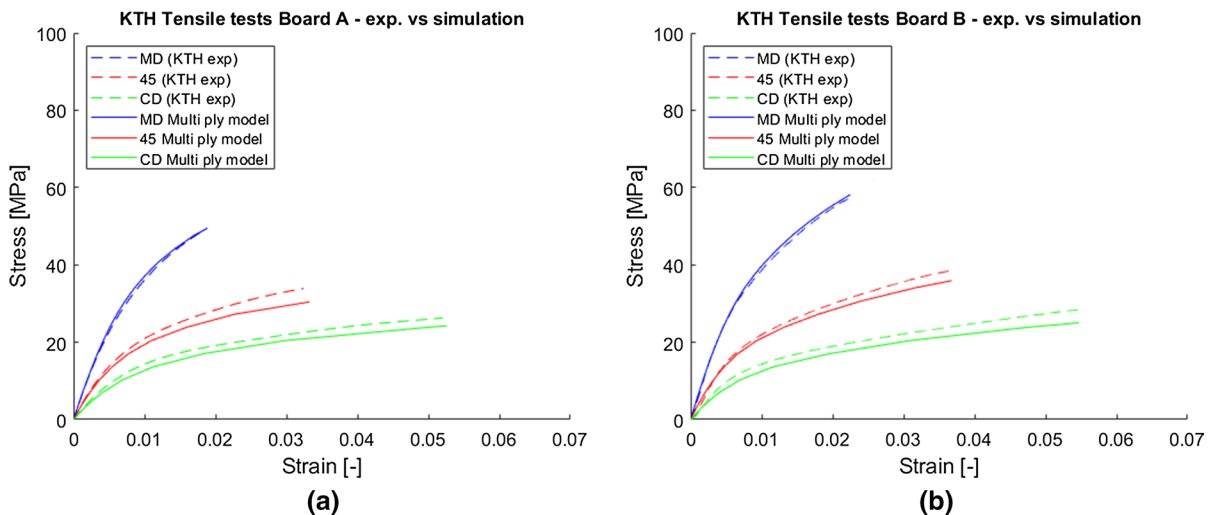
Fig. 12 The tensile tests compared with the numerical tensile tests of the three-ply model with individual thickness and material models for each ply. Note that damage is not included in the numerical models, i.e. the numerical tests were stopped when the actual strain-to-failure was researched
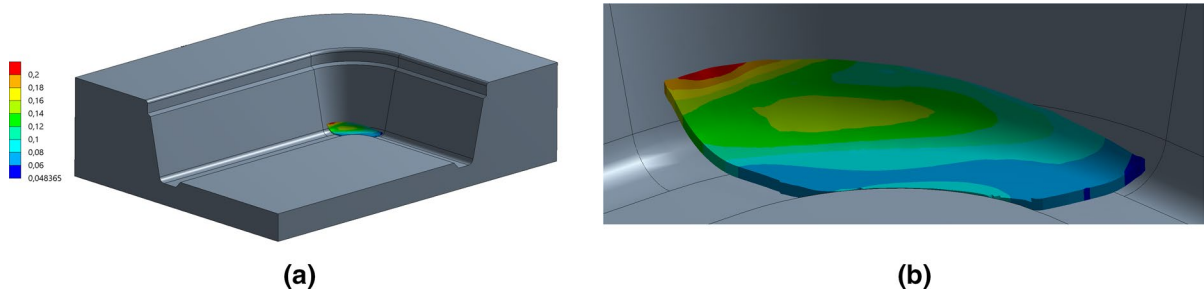
Fig. 13 The sub-model at end of the simulation. In **a** the position of the sub-model in the die is seen, and in **b** a close-up of the sub-model at the end of the simulation showing the total equivalent strain for the middle ply for Board A

expression in Eq. (8) along with the end value of the MD and CD curves in Fig. 8, i.e. the tensile stresses in MD and CD for each ply.

Numerical model

The numerical model developed and used for this study is a sub-model of the model used in Lindberg and Kulachenko (2021), where the lower critical area was successfully identified in the simulations of the full tray forming operation. The simulations in this study were performed with the finite element solver Ansys 2019R1 in a quasi-static regime using an implicit time-integration method. Due to the symmetry, a quarter model is simulated, as seen in Fig. 9. Initially, the blank is located so that the MD is parallel with the global x-axis and CD with the global y-axis. As the simulation starts, the punch presses the blank into the die and forms the tray.

The most critical area during the tray forming operation is the lower corner where the tray has been seen to fail during the forming operation (see Fig. 1). In order to resolve this part better with the simulation tools, a detailed sub-model was constructed which allowed: a) to use finer mesh density allowing to capture the strain gradients more accurately and b) resolve the individual plies. The area of the sub-model is about 1.3 cm² and is seen in Fig. 10a. In Fig. 10b the three parts included in the sub-model

simulation are viewed: the sub-section of the blank, the die, and the punch.

On the edges of the sub-model, the displacement and rotations from the global model are mapped onto the sub-model (see Fig. 11). I.e., the edges of the sub-model will deform in the same way as the corresponding locations deform in the global model. The remaining part of the sub-model is free to deform and will be influenced by, partly, the mapped boundary conditions on the edges, and mainly by the contact with the punch and, in the end, the contact with the die.

Results three-ply sub-model

Verification of three-ply model

For each of the total six plies, a non-linear orthotropic numerical material model is developed and fitted to the tensile tests of the individual tensile tests shown in Fig. 8. The stress–strain curves in a numerical tensile test are fitted to the actual test curves in an iterative process where the material parameters in the numerical model are changed until the fit between the numerical and actual tensile test curves is sufficient. The final fit between the ply tensile tests and the fitted material models are, as previously mentioned, shown in Appendix (Fig. 18).
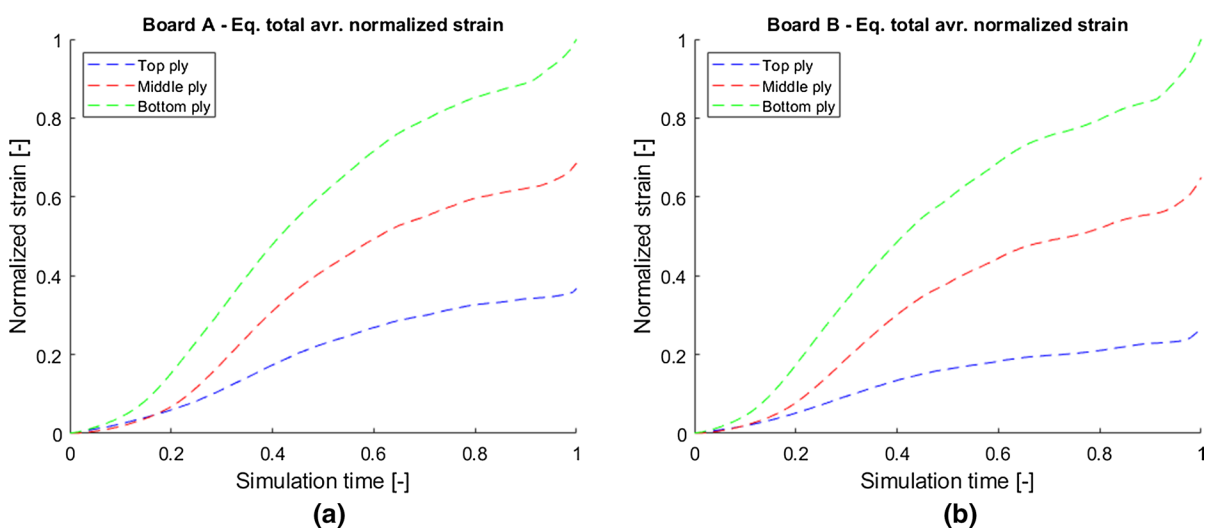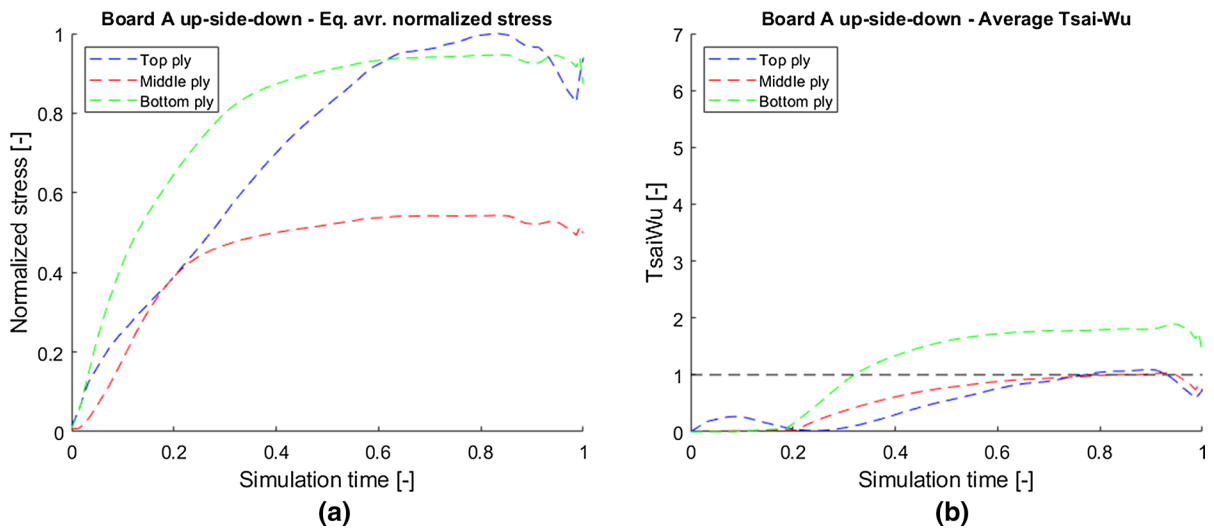

Fig. 14 The normalized equivalent total average strain over the section. In **a** for Board A, and in **b** for Board B
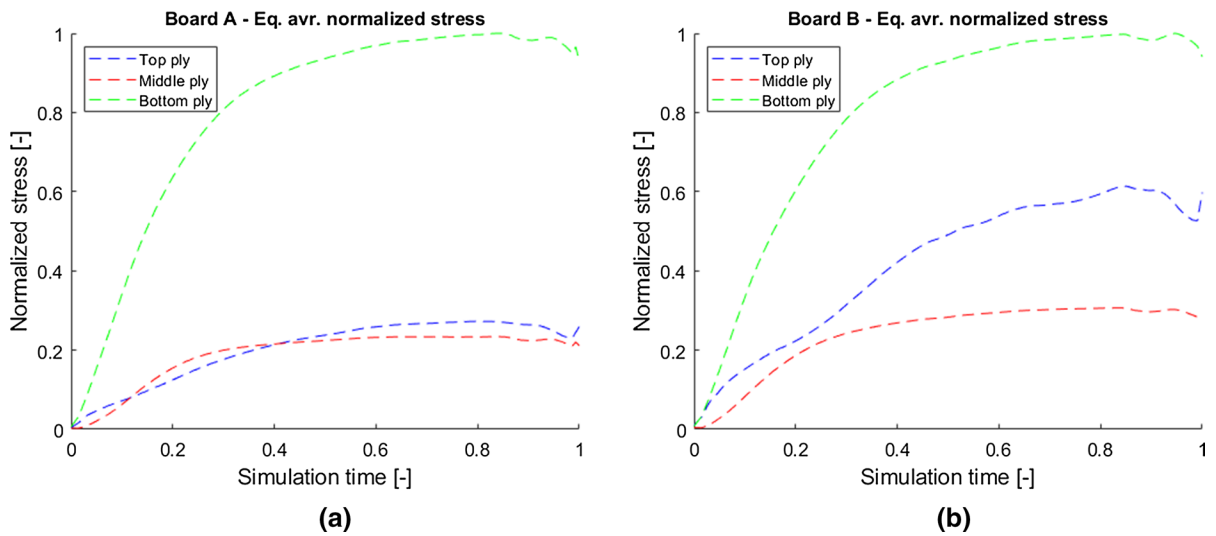
Fig. 15 The normalized equivalent average stress over the section. In **a** for Board A, and in **b** for Board B
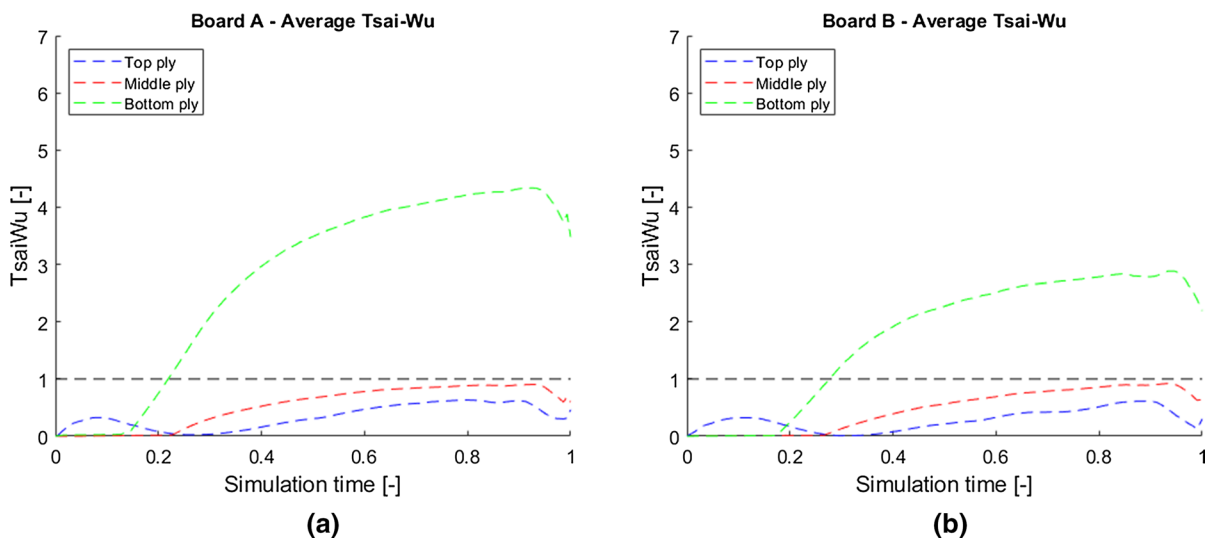
Fig. 16 The average Tsai-Wu index for each ply

Fig. 17 Results for the case where Board A is placed upside-down. In **a** the normalized equivalent stress, and in **b** the Tsai-Wu index

To verify the three-ply sub-model, the tensile tests of the full boards (Fig. 7) are compared to numerical tensile tests of a three-ply test specimen. I.e., the numerical test specimen has three different material models through the thickness, and each of the three plies has its individual thickness (see Table 1). The results are shown in Fig. 12.

As seen in Fig. 12, the experimental tensile tests and the numerical tensile tests agree well. Some differences, namely, underestimation of response from the multi-ply structure can be attributed to the damage introduced by the splitting process as well as the size effects mentioned early when none of the plies surpassed the strain to failure of the entire board.

Results from the three-ply sub-model

In Fig. 13 the deformed three-ply sub-model of the lower corner is seen at the end of the simulation, i.e. when the punch has pressed the paperboard down to the bottom of the die.

From the FE-models, we will first focus on the contribution to the load-bearing capacity by each ply. As the stress develops non-uniformly through the deformation process, we for each stress and strain quantity, chose to consider an evolution of the average stress and strain over the sub-model. Stresses and strains are calculated at the integration points. The values are then extrapolated to the nodes of the current element. As one node belongs to several elements, the value in the current node is an average of the extrapolated values from the integration points of the coinciding elements. Then, in turn, the average values of all nodes over the sub-model are used in the evaluation of the sub-model.

In Fig. 14 the total equivalent average strain of the section is shown. The values have been normalized by the highest value occurring for the respective board, which for both boards are the strain level in the bottom ply at the end of the forming operation. As seen, the bottom ply experiences the highest strain throughout the forming operation, and the

middle ply experience roughly 60% of that strain. For the strain in the top ply, there is a difference between the boards. For Board A, the strain level is, in relation to the strain in the bottom ply, higher than for Board B. This is natural, since the Board A top ply is more compliant in comparison to its bottom ply, and hence exhibits greater strain. The absolute values of the strain levels in the bottom plies are high, about 10% in the CD and 3% in MD for Board A, and 8% in CD and 3% in MD for Board B. Even though locally, much higher strains can exist than what is observed in a standard tensile test (Brandberg and Kulachenko 2020; Hagman and Nygårds 2012), these values are high. A possible contribution to that is not including the delamination in the model which can potentially decrease the strain in the critical area. Despite that, the relative difference between the board is still informative and is used in the discussion.

To show the load distributes between the plies we selected to compare the normalized stress levels. Figure 15 shows the normalized equivalent stress over the section for each ply. For each board, the stresses were normalized by dividing them by the highest stress value occurring, which is the stress in the bottom ply at a load factor (fictitious simulation time) of about 0.8. As seen, the Board B top ply takes a higher part of the load than the Board A top ply, which is natural since, the Board A top ply is more compliant, whilst the Board B top ply is stiffer in comparison to its bottom ply.

The results for the stress distributions are also visible for the failure criteria. In this work, the Tsai-Wu stress criterion (Tsai and Wu 1971) is used for the failure evaluation. The criterion states that the Tsai-Wu index should be below 1 to avoid failure. A detailed discussion about the Tsai-Wu index evaluation can be found in Lindberg and Kulachenko (2021). In Fig. 16, the Tsai-Wu index for each ply for the two boards is plotted. The Tsai-Wu index for the bottom ply is high for both boards. This is due to the high strains occurring in the bottom plies, as previously discussed. Based on these results, we can conclude that the failure initiates in the bottom ply, and that the Tsai-Wu index is higher for Board A than

for Board B, which agrees with the observed performances of the considered boards.

To investigate the effect of ply properties on the failure, the stress distribution and the failure criteria were investigated for the case when Board A was placed up-side-down in the tray forming operation. This, in fact, was tested in a pilot test and resulted in a better performance of Board A. In Fig. 17 the outcome of placing Board A up-side-down in the numerical three-ply model is shown. The results are surprising since the top ply and bottom ply end up having the same stress levels. This "unloading" of the bottom ply has a direct impact on the risk of failure, which is seen in Fig. 17b, where the Tsai-Wu index decreases by 60% as compared to the original case for Board A, see Fig. 16a. This practically implies that due to the high strains in the bottom ply, it is better to have a less stiff ply in the bottom and at the same have a stiffer top ply to take a greater part of the load, hence protecting the bottom ply. In other words, there is an advantage of having the refining energies more balanced than they currently are for Board A.

Conclusions

The three-ply FE sub-model used in this project revealed the critical difference between the considered commercial boards when it comes to their performances in the tray forming operation. Although the boards did not show a significant difference in mechanical properties when tested by a conventional method on sheet level, they did show significant discrepancies in mechanical properties when split and tested ply-wise. This difference can solely be explained by dissimilar refining energies used in the constituent pulp.

The results from the three-ply sub-model suggest that the highest strains occur in the bottom ply for both boards, that is, the ply that faces the die. Furthermore, it is seen that the risk of failure increases drastically when the top ply is weakened as the load-bearing function is shifted toward the bottom ply. In fact, with the board having non-uniform strength and

stiffness profile through the thickness, it is advantageous to place the weaker side of the board away from the punch in the considered configuration, which is not very intuitive.

There are some limitations of the study that could affect the results. One is that the results in the sub-model are directly dependent on the boundary conditions mapped from the model in Lindberg and Kulachenko (2021). As discussed in that study, the model is conservative and does not account for delamination in the creased areas leading to higher strain levels than those encountered in reality. Furthermore, the rate dependency is not considered, and all the material parameters were obtained in the tensile tests performed at a low rate, but the tray forming operation for a 25 mm deep tray takes less than a second. Further, the effect of the tool temperature is not explicitly accounted for. Lastly, as the paperboard is split into its plies, the thickness which the splitting machine will use, must be set. This is set to the intended value of the ply in the papermaking process. However, as seen in Table 1, the standard deviation of the ply thickness can be as much as 13%, meaning that it is possible that the transition between the plies is not exactly at the position where splitting occurs. Hence, small frations of the material from the adjacent layer can be included, possibly rending in the tensile test curves showing different stiffness of the plies compared to what is in fact the case for the individual plies. In the simulations, we used the mean thickness of the plies extracted during splitting.

Despite these limitations which prevent accurate estimations of the stress levels, the comparative study clearly shows the importance of including multi-ply structure in simulating converting operations and demonstrates the degrees of freedom which can be used in optimizing the board structure.

Declarations

Appendix

A1 Material model fit for each ply

See Fig. 18.
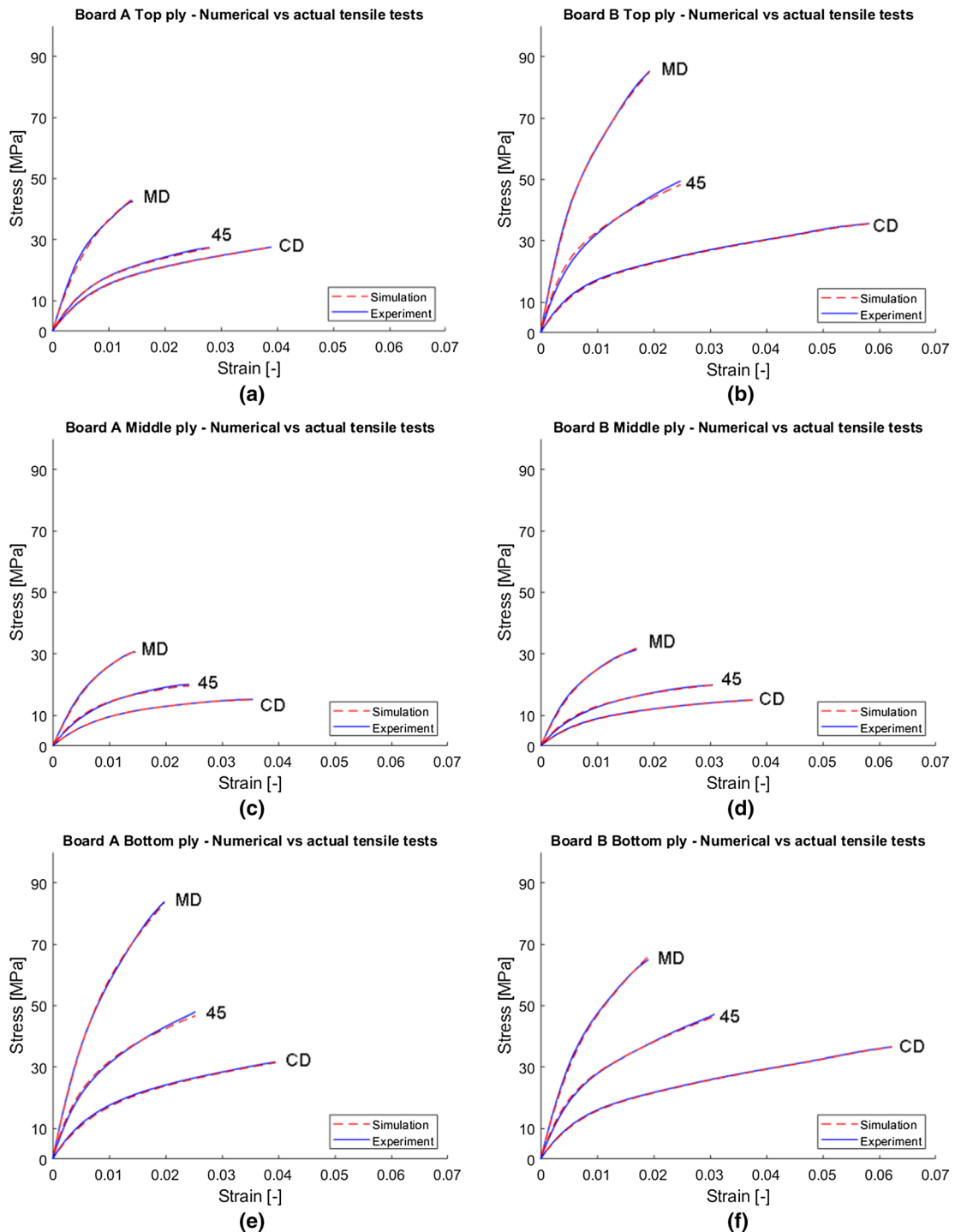
Fig. 18 The fitting of the numerical material models to the actual tensile tests for each ply. The failure stress in compression is numerically set to be 50% of that in tension, which is demonstrated in the figures. Note that damage is not included in the model but is instead a part of the post-processing

A2 Tensile tests for each ply per direction vs full board

See Fig. 19.
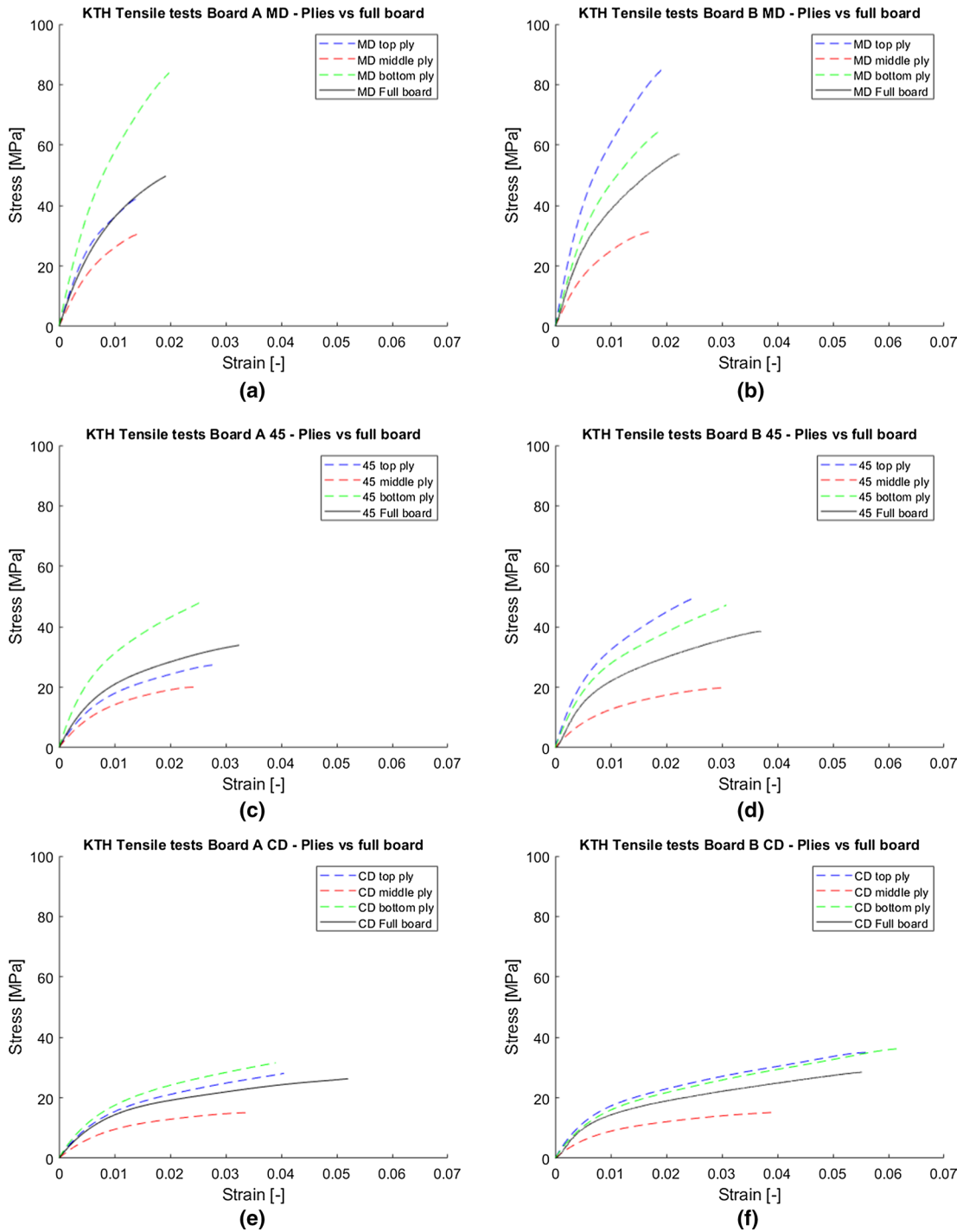
Fig. 19 Tensile tests per direction: The full paperboards together with the individual plies. As seen, except for the CD direction for Board B (**f**), the full board has a higher strain to failure than the individual plies. The reasons are discussed in the Material and Method section

A3 Results from fiber characterization performed by PulpEye

PulpEye is a tool for quantifying the geometric properties of the fibers in the pulp before going into the paperboard machines. It is placed after the complete refining process. The PulpEye at Holmen Iggesund measures the fiber length, projected length (the so-called p-length) and the fiber widths. The p-length is the shortest distance between the ends of each fiber. By using the p-length, the curl index can be computed as (fiber length/p-length) − 1. With the measured data, statistical information about the fibers can be determined, such as the distribution curves and mean values for the fiber length, curl and width.

The mixture for the top and bottom plies is 40% softwood and 60% hardwood. For the middle plies the mixture is different, namely 30% softwood and then 70% reused, so called "broke", fibers that have been recovered from the spill from the paperboard machine. The broke fibers consist in turn of 50% softwood and 50% hardwood.

The data received for the Board A pulp was measured at a location after that the hardwood and softwood had been refined together. However, the Board B pulp was measured before the softwood and hardwood pulps were mixed, as the pulp extraction after the mixture is not possible. Hence, to get the mixed and final pulp data for the Board B plies, the mixture of the softwood and hardwood pulp had to be done by combining the data files for the individual plies. This was done by taking 40% of the data from the softwood data files, and 60% from the hardwood data files and then creating a new data file which then was used to study the distributions and the mean values

of the fiber length, curl and width. This brings some uncertainties about the final data since the weighing of 40% softwood and 60% hardwood in production is based on dry weight, rather than the number of fibers. This could imply that the mean values and the length weighted mean value for the fiber lengths for the Board B plies should be somewhat greater than seen in this report.

In Figs. 20, 21 and 22 the results from the PulpEye measurement are shown. Note that, as previously explained, the mixing of the Board B pulp has been done manually for this report by combining 40% of the data from the softwood data file with 60% of the hardwood data file, since no measuring took place with PulpEye on the final pulp going into the machine. Hence the results for the Board B pulp must be interpreted with some cautiousness.

The general trend is that the distributions follow each other fairly well. No big deviations are observed. The modes for the fiber length, curl and fiber width are approximately the same for all curves. In Table 6 the mean values for the length, curl and width are shown for the top and middle plies. The middle plies are shown in a separate table (Table 7) since they have a different mixture.

Even though the data must be interpreted with some cautiousness, the results for the length weighted fiber length mean values are in line with the registered refining energies. The Board A top ply has considerably lower refining energy than for its bottom ply, leading to a somewhat higher length weighted fiber length mean compared to the bottom ply. The bottom ply value, 1.09 mm, is however very low and is closer to an 80%/20% hardwood/softwood combination in the pulp, something discussed in the project
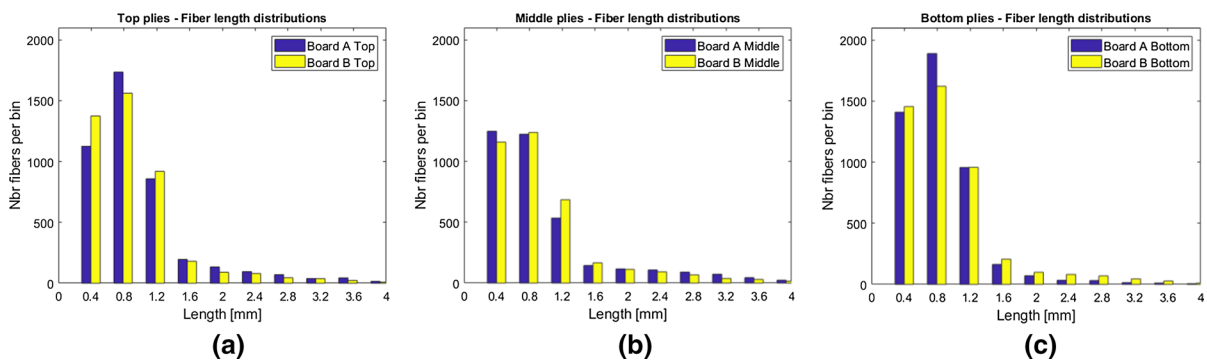
Fig. 20 Distribution of the fiber length for the three plies for each paperboard
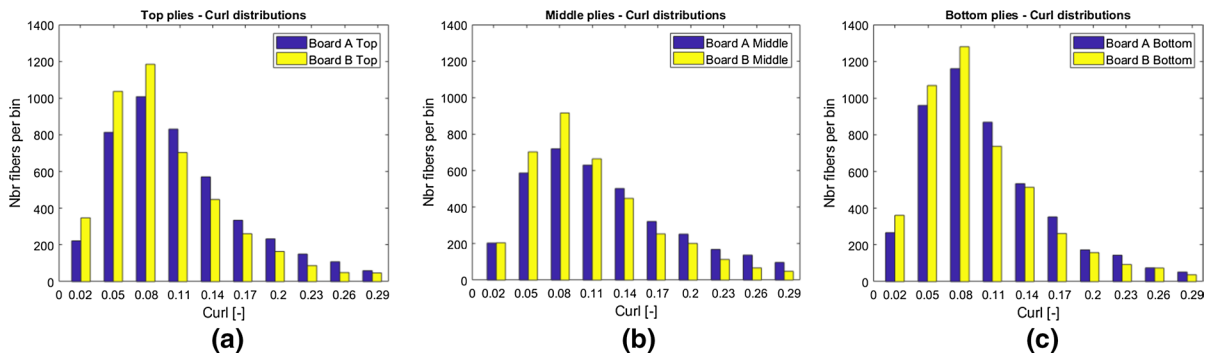
Fig. 21 Distribution of the curl index for the three plies for each paperboard
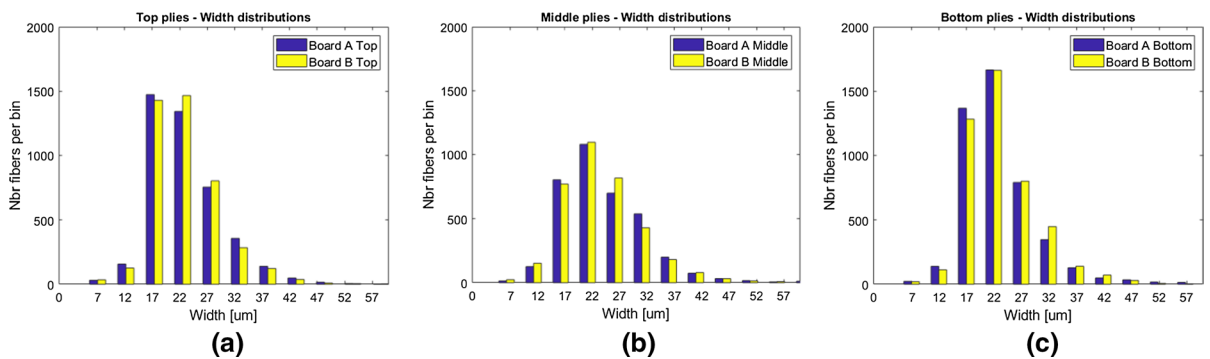
Fig. 22 Distribution of the fiber width for the three plies for each paperboard

Table 6 Mean values from the PulpEye measurements for the top and bottom plies (hardwood/softwood = 60%/40%)

Ply	Fiber length: mean (mm)	Fiber length: length weighted mean (mm)	Curl mean (-)	Width mean (um)
Board A top	0.97	1.43*	0.11	23.2
Board B top	0.89	1.30	0.10	23.2
Board A bottom	0.82	1.09**	0.10	22.8
Board B bottom	0.92	1.35	0.10	23.3

*Softwood refiner logged for low energies on several occasions during the time for the measurement

**Possibly erroneous measurement representing 80%/20% hardwood/softwood rather than 60%/40%

team. A more regular 60/40 hardwood/softwood combination should give a value around 1.3 mm for the length weighted fiber length mean.

The difference in refining energies for Board B also gives a slightly lower length weighted length mean for the top ply compared to the bottom ply. The middle plies show greater values for the length weighted mean, which is partly due to their low refining energies and different mixture.

Table 7 Mean values from the PulpEye measurements for the middle plies (hardwood/"broke 50/50" = 30%/70%)

Ply	Fiber length: mean (mm)	Fiber length: length weighted mean (mm)	Curl mean (-)	Width mean (um)
Board A middle	0.98	1.59	0.12	24.1
Board B middle	0.96	1.48	0.11	23.6

References

Alajami A, Li Y, Simon JW (2018) Modelling the anisotropic in-plane and out-of-plane elastic-plastic response of paper. PAMM 18:e201800322. https://doi.org/10.1002/pamm.201800322

Alzweighi M, Mansour R, Tryding J, Kulachenko A (2021) Evaluation of Hoffman and Xia plasticity models against bi-axial tension experiments of planar fiber network materials. Int J Solids Struct. https://doi.org/10.1016/j.ijsolstr.2021.111358

Awais M, Sorvari J, Tanninen P, Leppänen T (2017) Finite element analysis of the press forming process. Int J Mech Sci 131:767–775. https://doi.org/10.1016/j.ijmecsci.2017.07.053

Baum GA, Habeger CC, Fleischman EH (1982) Measurement of the orthotropic elastic constants of paper. https://smartech.gatech.edu/bitstream/handle/1853/2848/tps-117.pdf?isAllowed=y&sequence=1

Bedzra R, Li Y, Reese S, Simon J-W (2019) A comparative study of a multi-surface and a non-quadratic plasticity model with application to the in-plane anisotropic elastoplastic modelling of paper and paperboard. J Compos Mater 53:753–767. https://doi.org/10.1177/0021998318790656

Brandberg A, Kulachenko A (2020) Compression failure in dense non-woven fiber networks. Cellulose 27:6065–6082. https://doi.org/10.1007/s10570-020-03153-2

Chen F-K, Lin S-Y (2007) A formability index for the deep drawing of stainless steel rectangular cups. Int J Adv Manuf Technol 34:878. https://doi.org/10.1007/s00170-006-0659-3

Didone M, Saxena P, Brilhuis-Meijer E, Tosello G, Bissacco G, McAloone TC, Pigosso DCA, Howard TJ (2017) Moulded pulp manufacturing: overview and prospects for the process technology. Packag Techno Sci 30:231–249. https://doi.org/10.1002/pts.2289

Fellers C, de Ruvo A, Elfstrom J, Htun M (1980) Edgewise compression properties—A comparsion of handsheets made from pulps of various yields. Tappi 63:109–112

Fellers C, Westerlind B, De Ruvo A (1983) An investigation of the biaxial failure envelope of paper–experimental study and theoretical analysis. In: Proceedings of fundamental research symposium, Cambridge, pp 527–59.

Gill YQ, Jin J, Song M (2020) Comparative study of carbon-based nanofillers for improving the properties of HDPE for potential applications in food tray packaging. Polym Polym Compos 28:562–571. https://doi.org/10.1177/0967391119892091

Hagman A, Timmermann B, Nygårds M, Lundin A, Barbier C, Fredlund M, Östlund S (2017) Experimental and numerical verification of 3D forming. In: 6th Fund Research Symp. Pembroke College, Oxford, England, pp 3–26. URL: https://bioresources.cnr.ncsu.edu/resources/experimental-and-numerical-verification-of-3d-forming/

Hagman A, Nygårds M (2012) Investigation of sample-size effects on in-plane tensile testing of paperboard. Nord Pulp Paper Res J 27:295–304. https://doi.org/10.3183/NPPRJ-2012-27-02-p295-304

Harrysson A, Ristinmaa M (2008) Large strain elasto-plastic model of paper and corrugated board. Int J Solids Struct 45:3334–3352. https://doi.org/10.1016/j.ijsolstr.2008.01.031

Hauptmann M, Wallmeier M, Erhard K, Zelm R, Majschak J-P (2015) The role of material composition, fiber properties and deformation mechanisms in the deep drawing of paperboard. Cellulose 22:3377–3395. https://doi.org/10.1007/s10570-015-0732-x

Hill R (1948) A theory of the yielding and plastic flow of anisotropic metals. Proc R Soc A Math Phys Eng Sci 193:281–297

Hristopulos DT, Uesaka T (2004) Structural disorder effects on the tensile strength distribution of heterogeneous brittle materials with emphasis on fiber networks. Phys Rev B 70:064108. https://doi.org/10.1103/PhysRevB.70.064108

I'Anson S, Sampson W, Savani S (2008) Density dependent influence of grammage on tensile properties of handsheets. J Pulp Pap Sci 34:182

Jele TB, Lekha P, Sithole B (2021) Role of cellulose nanofibrils in improving the strength properties of paper: a review. Cellulose. https://doi.org/10.1007/s10570-021-04294-8

Kulachenko A, Uesaka T (2012) Direct simulations of fiber network deformation and failure. Mech Mater 51:1–14. https://doi.org/10.1016/j.mechmat.2012.03.010

Laukala T, Ovaska S-S, Tanninen P, Pesonen A, Jordan J, Backfolk K (2019) Influence of pulp type on the three-dimensional thermomechanical convertibility of paperboard. Cellulose 26:3455–3471. https://doi.org/10.1007/s10570-019-02294-3

Leminen V, Matthews S, Pesonen A, Tanninen P, Varis J (2018a) Combined effect of blank holding force and forming force on the quality of press-formed paperboard trays. Procedia Manuf 17:1120–1127. https://doi.org/10.1016/j.promfg.2018.10.026

Leminen V, Matthews S, Tanninen P, Varis J (2018b) Effect of creasing tool dimensions on the quality of press-formed paperboard trays. Procedia Manuf 25:397–403. https://doi.org/10.1016/j.promfg.2018.06.109

Leminen V, Tanninen P, Pesonen A, Varis J (2019) Effect of mechanical perforation on the press-forming process of paperboard. Procedia Manuf 38:1402–1408. https://doi.org/10.1016/j.promfg.2020.01.148

Leminen V, Tanninen P, Matthews S, Niini A (2020) The effect of heat input on the compression strength and durability of press-formed paperboard trays. Procedia Manuf 47:6–10. https://doi.org/10.1016/j.promfg.2020.04.108

Li Y, Stapleton SE, Reese S, Simon J-W (2016) Anisotropic elastic-plastic deformation of paper: in-plane model. Int J Solids Struct 100:286–296. https://doi.org/10.1016/j.ijsolstr.2016.08.024

Li S, Sitnikova E, Liang Y, Kaddour A-S (2017) The Tsai-Wu failure criterion rationalised in the context of UD composites. Compos Part A Appl Sci Manuf 102:207–217. https://doi.org/10.1016/j.compositesa.2017.08.007

Lindberg G, Kulachenko A (2021) Tray forming operation of paperboard: a case study using implicit finite element analysis. Packag Technol Sci. https://doi.org/10.1002/pts.2619

Linvill E, Wallmeier M, Östlund S (2017) A constitutive model for paperboard including wrinkle prediction and post-wrinkle behavior applied to deep drawing. Int J Solids Struct 117:143–158. https://doi.org/10.1016/j.ijsolstr.2017.03.029

Motamedian HR, Halilovic AE, Kulachenko A (2019) Mechanisms of strength and stiffness improvement of paper after PFI refining with a focus on the effect of fines. Cellulose 26:4099–4124. https://doi.org/10.1007/s10570-019-02349-5

Niini A, Tanninen P, Varis J, Leminen V (2021) Effects of press-forming parameters on the dimensional stability of paperboard trays. BioResources 16:4876. https://doi.org/10.15376/biores.16.3.4876-4890

Östlund S (2017) Three-dimensional deformation and damage mechanisms in forming of advanced structures in paper. In: Batchelor W, Söderberg D (eds) Adv in pulp and paper research, Trans of the 16th Fund Research Symp. Oxford, pp 489–594. URL: https://bioresources.cnr.ncsu.edu/resources/three-dimensional-deformation-and-damage-mechanisms-in-forming-of-advanced-structures-in-paper/

Ovaska S-S, Geydt P, Leminen V, Lyytikäinen J, Matthews S, Tanninen P, Wallmeier M, Hauptmann M, Backfolk K (2018) Three-dimensional forming of multi-layered materials: material heat response and quality aspects. J Appl Packag Res 10:3

Reddy MV, Reddy PV, Ramanjaneyulu R (2019) Effect of heat treatment and sheet thickness on deep drawing formability: a comparative study. Int J Appl Eng Res 14:802–805

Rhim J-W (2010) Effect of moisture content on tensile properties of paper-based food packaging materials. Food Sci Biotechnol 19:243–247. https://doi.org/10.1007/s10068-010-0034-x

Robertsson K, Borgqvist E, Wallin M, Ristinmaa M, Tryding J, Giampieri A, Perego U (2018) Efficient and accurate simulation of the packaging forming process. Packag Technol Sci 31:557–566. https://doi.org/10.1002/pts.2383

Rojek J, Kleiber M, Piela A, Stocki R, Knabel J (2004) Deterministic and stochastic analysis of failure in sheet metal forming operations. Steel Grips 2:29–34

Scandinavian Pulp, Paper and Board testing committee (2001) SCAN-P 88:01. Stockholm

Siracusa V, Rocculi P, Romani S, Dalla Rosa M (2008) Biodegradable polymers for food packaging: a review. Trends Food Sci Technol 19:634–643. https://doi.org/10.1016/j.tifs.2008.07.003

Suhling J, Rowlands R, Johnson M, Gunderson D (1985) Tensorial strength analysis of paperboard. Exp Mech 25:75–84. https://doi.org/10.1007/Bf02329129

Tanninen P, Leminen V, Matthews S, Kainusalmi M, Varis J (2018) Process cycle optimization in press forming of paperboard. Packag Techno Sci 31:369–376. https://doi.org/10.1002/pts.2331

Tanninen P, Leminen V, Pesonen A, Matthews S, Varis J (2020) Surface fracture prevention in paperboard press forming with advanced force control. Procedia Manuf 47:80–84. https://doi.org/10.1016/j.promfg.2020.04.140

Tjahjanto DD, Girlanda O, Östlund S (2015) Anisotropic viscoelastic–viscoplastic continuum model for high-density cellulose-based materials. J Mech Phys Solids 84:1–20. https://doi.org/10.1016/j.jmps.2015.07.002

Tsai SW (1984) A survey of macroscopic failure criteria for composite materials. J Reinf Plast Compos 3:40–62. https://doi.org/10.1177/073168448400300102

Tsai SW, Wu EM (1971) A general theory of strength for anisotropic materials. J Compos Mater 5:58–80. https://doi.org/10.1177/002199837100500106

Vishtal A, Retulainen E (2012) Deep-drawing of paper and paperboard: the role of material properties. BioResources 7:4424–4450

Vishtal A, Retulainen E, Khakalo A, Rojas OJ (2015) Improving the extensibility of paper: sequential spray addition of gelatine and agar. Nord Pulp Paper Res J 30:452–460. https://doi.org/10.3183/npprj-2015-30-03-p452-460

Wallmeier M, Linvill E, Hauptmann M, Majschak J-P, Östlund S (2015) Explicit FEM analysis of the deep drawing of paperboard. Mech Mater 89:202–215. https://doi.org/10.1016/j.mechmat.2015.06.014

Wang J, Wang L, Gardner DJ, Shaler SM, Cai Z (2021) Towards a cellulose-based society: opportunities and challenges. Cellulose. https://doi.org/10.1007/s10570-021-03771-4

Xia QS, Boyce MC, Parks DM (2002) A constitutive model for the anisotropic elastic–plastic deformation of paper and paperboard. Int J Solids Struct 39:4053–4071. https://doi.org/10.1016/S0020-7683(02)00238-X